Reliable Euler deconvolution estimates throughout the vertical derivatives of the total-field anomaly

Felipe F. Melo [*], Valéria C.F. Barbosa

Observatório Nacional, Department of Geophysics, General José Cristino Street, 77, São Cristóvão, 20921-400, Rio de Janeiro, Rio de Janeiro, Brazil

ABSTRACT

We propose a novel methodology to select reliable Euler deconvolution estimates throughout the vertical derivatives of the total-field anomaly, grounded on the capability of this quantity to locate anomalies due to its higher signal decay with distance. In applying Euler deconvolution to a small moving-data window, we compute the standard deviation of the vertical derivatives of the total-field anomaly for each data window. Then, we define the reliable source-location estimates as those estimates that are obtained by using the data windows with the largest standard deviations of the vertical derivatives of the total-field anomaly. For all tentative values of the structural index (SI), the reliable estimates with tight clustering define the correct SI and the mean of these estimates define the source position. We compared our methodology to select reliable Euler source-position estimates with two available methodologies in the literature based on the rejection criteria of data amplitude and of depth uncertainty. We conducted tests on synthetic noise-corrupted data to investigate the sensitivity of our method to deal with the presence of: i) an additive nonlinear background that simulates a regional field; ii) interfering anomalies with distinct amplitudes; iii) weak-, mid-, and strong-interfering anomalies; and iv) distinct noise levels. Most of tests in the sensitivity analysis shows that our methodology to select reliable Euler source-position estimates yielded better interpretation of the simulated magnetic sources than the methodology based on the rejection criteria of data amplitude and of depth uncertainty. The only exception was the tests with high noise levels in which the reliable Euler estimates selected either by our method or by the rejection criteria yielded poor interpretations. Applications to a real aeromagnetic survey from southern Brazil interpreted an isolated plug intrusion over the Anitápolis anomaly and a swarm of shallow-seated dikes with northwest-southeast trend over the Paranaguá Terrane.

1. Introduction

Euler deconvolution (Reid et al., 1990; Barbosa et al., 1999) is the most popular technique for fast interpretation of potential-field data. It works with potential-field measurements, their gradients, and a given integer number called the structural index (SI), which in turn depends on the nature (type) of the geologic source (Reid et al., 2014; Reid and Thurston, 2014). Mathematically, Euler deconvolution assumes a tentative SI, solves a system of equations in a moving-data window scheme and estimates the four parameters: base level, horizontal and vertical positions of a geologic source.

Traditionally, for each tentative SI, one map is generated where the estimates of the source horizontal and vertical coordinates obtained by Euler deconvolution are plotted. Specifically, the estimates of the source

horizontal coordinates are plotted in the plan view ($x - y$ plane) of the study area (Reid et al., 1990), and usually the source depth (vertical coordinates) estimates are plotted in different color or size. In this case, base-level estimates are computed but usually neglected. When the correct SI is used the estimates cluster over the source (Thompson, 1982). Barbosa et al. (1999) and Silva and Barbosa (2003) presented the analytical estimators for the horizontal and vertical source positions in Euler deconvolution. They show that over the anomaly, the estimates of the horizontal source position are very close to the respective true source horizontal coordinates regardless of the used SIs. Barbosa et al. (1999) and Silva and Barbosa (2003) also show that the estimate of the source depth and the SI are linearly dependent. The greater the SI, the greater is the estimate of the source depth via Euler deconvolution.

The cumbersome with the classic plot is the large amount of solutions

---

(Barbosa and Silva, 2011). In order to deal with the spray of solutions and define the correct SI some authors developed some criteria, e.g., Thompson (1982) and Reid et al. (1990) accept solutions based on the depth uncertainty. Fairhead et al. (1994) computed the maximum of the horizontal gradient of the reduced-to-the-pole anomaly to accept solutions. Mikhailov et al. (2003) and Ugalde and Morris (2010) filtered solutions using clustering techniques based on artificial intelligence and fuzz c-means, respectively. FitzGerald et al. (2004) provided an overview on best practices to select the solutions and proposed new ones for the extended Euler technique (Mushayandebvu et al., 2001; Nabighian and Hansen, 2001). The FitzGerald et al.'s (2004) overview totalizes 17 discrimination techniques aiming to select the more reliable Euler solutions considering distinct SIs. The large amount of discrimination techniques presented by FitzGerald et al. (2004) show the complexity of distinguishing reliable Euler solutions from spurious ones considering distinct geologic scenarios. Uieda et al. (2013, 2014) adapted the solution from Beiki and Pedersen (2010) ranking the solutions based on the estimated error computed from all parameters. Alternatively, Silva and Barbosa (2003), Melo et al. (2013), and Melo and Barbosa (2018) plot all estimates separately against the central position of the moving-data window, resulting in four maps, one for each estimate. In this procedure, there is no need to select reliable estimates or deal with the spray of solutions because all solutions are plotted.

Some free codes are available to perform Euler deconvolution. For profile data and not open source, Durrheim and Cooper (1998) estimated the position and base level and Cooper (2006) obtained the dip and susceptibility from dikes with a modified version using the Hough transform. For gridded data and not open source code, FitzGerald et al. (2004) implemented the extended Euler. For gridded data and open source codes, Gerovska and Araúzo-Bravo (2003) estimated the position and the SI based on the properties of the differential similarity transformation and Uieda et al. (2013, 2014) estimated the source position and the base level in the standard way. The extended Euler (Mushayandebvu et al., 2001; Nabighian and Hansen, 2001), implemented by FitzGerald et al. (2004), assumes a new system of equations with the Hilbert transform. In this new system, the base level is set to zero, as the result of the Hilbert transform of a constant.

In this work, we analyze Euler deconvolution solutions selecting the reliable estimates throughout the moving-data windows with the largest standard deviations of the vertical derivatives of the total-field anomaly. Synthetic tests show the robustness of our methodology to: i) select reliable Euler estimates; ii) determine the SI correctly; and iii) locate the source positions. These synthetic tests are produced by: i) isolated sources in the presence of a nonlinear background simulating a regional field; ii) multiple anomalies with distinct amplitude; iii) interfering anomalies; and iv) noisy data. We compare the outcomes of the synthetic and real data applications of our methodology to two available methodologies in the literature (FitzGerald et al., 2004) to define reliable solutions based on the amplitude of the data and on depth uncertainty. Our methodology yields better results than the two available methodologies to pick out reliable Euler solutions. All methodologies fail in one test with magnetic data corrupted by high noise levels. To our knowledge, neither methodology is able to deal with data contaminated with high noise level in Euler deconvolution. The field results from the aeromagnetic data, southern Brazil, suggest that a single plug intrusion generates the Anitápolis anomaly and a set of northwest-southeast trending dikes is defined in the Paranaguá Terrane.

2. Theory

Let us adopt a right-handed Cartesian coordinate system with the x-axis pointing to north, the y-axis pointing to east, and with the z-axis pointing downward. Reid et al. (1990) defined the Euler deconvolution as:

$$(x - x_o)\frac{\partial h}{\partial x} + (y - y_o)\frac{\partial h}{\partial y} + (z - z_o)\frac{\partial h}{\partial z} = \eta(b - h), \tag{1}$$

where x_o, y_o and z_o are the source positions, x, y and z are the observation positions, $h = h(x, y, z)$ is the total-field anomaly and $\partial h/\partial x$, $\partial h/\partial y$ and $\partial h/\partial z$ are its gradients with respect to the variables x, y and z, respectively. In Eq. (1), η is an integer number, named structural index (SI), which depends on the source type and b is a base level or data background.

By applying Euler deconvolution with a moving-data window scheme using a tentative value of SI, we obtain the estimated parameters $\hat{x}_o^k$ and $\hat{y}_o^k$ (horizontal source positions), $\hat{z}_o^k$ (vertical source position) and $\hat{b}^k$ (base level), for the kth position of the moving-data window. Hence, Eq. (1) can be written as:

$$\hat{x}_o^k\frac{\partial h_j}{\partial x} + \hat{y}_o^k\frac{\partial h_j}{\partial y} + \hat{z}_o^k\frac{\partial h_j}{\partial z} + \eta\hat{b}^k = x_j\frac{\partial h_j}{\partial x} + y_j\frac{\partial h_j}{\partial y} + z_j\frac{\partial h_j}{\partial z} + \eta h_j, \tag{2}$$

where the subscript j is related to the jth observation position (x_j, y_j, z_j) inside the kth moving-data window. The estimates $\hat{x}_o^k$, $\hat{y}_o^k$, $\hat{z}_o^k$ and $\hat{b}^k$ in each kth position of the moving-data window are the Euler solutions to be visualized by assuming a tentative SI.

In matrix form, the solution of the linear system of equations described in Eq. (2), for each kth position of the moving-data window via the least-squares method is:

$$\mathbf{p}^k = \left(\mathbf{A}^{k\mathrm{T}}\mathbf{A}^k\right)^{-1}\mathbf{A}^{k\mathrm{T}}\mathbf{d}^k, \tag{3}$$

where $\mathbf{p}^k$ is the estimated parameter vector with the four estimates ($\hat{x}_o^k$, $\hat{y}_o^k$, $\hat{z}_o^k$ and $\hat{b}^k$), $\mathbf{A}^k$ is the $M \times 4$ sensitivity matrix whose elements of the jth row are: $a_{j1}^k = (\partial h_j/\partial x)$, $a_{j2}^k = (\partial h_j/\partial y)$, $a_{j3}^k = (\partial h_j/\partial z)$ and $a_{j4}^k = \eta$, $j = 1, \ldots, M$ where M is the number of observations in a moving-data window. The jth element of the M-dimensional data vector $\mathbf{d}^k$ is $d_j^k = x_j(\partial h_j/\partial x) + y_j(\partial h_j/\partial y) + z_j(\partial h_j/\partial z) + \eta h_j$. In Eq. (3), the superscript T stands for transposed.

3. Method

To perform the Euler deconvolution the derivatives of the gridded potential-field data are computed in Fourier domain (Blakely, 1996, p. 324). However, measured gradient data can be used if available (Schmidt et al., 2004). In cases of low signal to noise ratio, the filtering of random noise can be achieved prior to run the Euler deconvolution in space domain (Minty, 1991; Mauring and Kihle, 2006), in Fourier domain (Jacobsen, 1987; Minty, 1991) or in wavelet domain (Ridsdill-Smith and Dentith, 1999; Leblanc and Morris, 2001; Fedi and Florio, 2003). Pašteka et al. (2009) propose an alternative approach and regularize the noisy derivatives employed in Euler deconvolution. Florio et al. (2014) show that the denoising should be carefully employed because improperly denoised data also lead to wrong depth estimates in Euler deconvolution. On applying the Euler deconvolution, the data window is moved over the whole data grid and, at each position of data window, the four Euler estimates ($\hat{x}_o^k$, $\hat{y}_o^k$, $\hat{z}_o^k$ and $\hat{b}^k$ in Eq. (3)) are obtained. We follow the recommendations of Reid et al. (2014) regarding the size of the moving-data window related to the grid space and depth of investigation. These authors stated that the window size must be at least twice the measured data grid interval and greater than half the desired depth of investigation.

In this work, we introduce a novel criterion to distinguish reliable Euler solutions from spurious ones. We keep only a percentage of the moving-data windows ranked by the largest standard deviations of the vertical derivatives of the total-field anomaly (third column of the sensitivity matrix in Eq. (3)). This is achieved, in the kth window, by
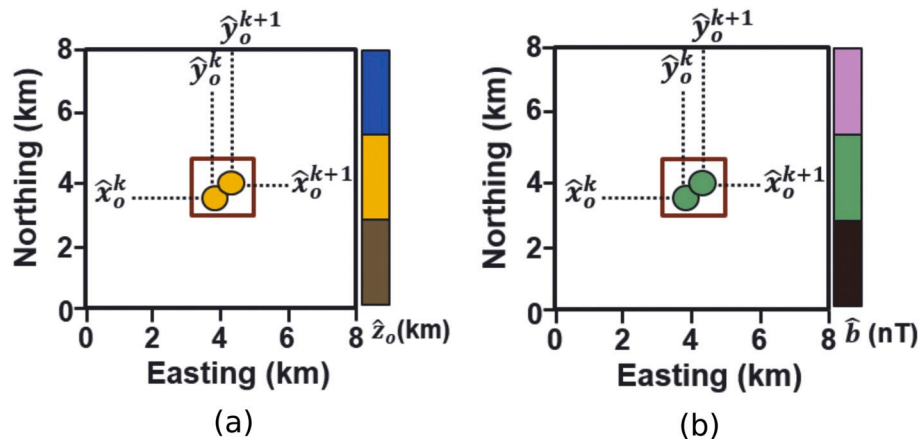
computing the sample standard deviation (Gubbins, 2004, pp. 94) of the vertical derivatives of the total-field anomaly:

$$s^k = \sqrt{\frac{\sum_{j=1}^{M}\left(a_{j3}^k - \mu^k\right)^2}{M-1}}, \tag{4}$$

where μ^k is the mean of the vertical derivatives of the total-field anomaly in the kth window. Next, we select the moving-data windows with the largest standard deviations and plot the corresponding Euler solutions for each tentative SI on distinct plots. The percentage of moving-data windows selected is defined based on the dataset; this selection is accomplished by decreasing the amount of selected solutions until a cluster is defined over an anomaly. The reliable selected estimates lie over the sources, thus reducing the spray of solutions. The best SI is the one that produces the tightest cluster of the source-position or the base-level estimates. Finally, the mean of depth estimates defines the optimum depth to the top or to the center of the source.

The physical basis to the choice of reliable Euler solutions related to the data windows with largest standard deviations of the vertical derivative of the total-field anomaly is its ability to locate interfering anomalies due to its higher signal decay with distance. In the interpretation of non-interfering anomalies via Euler deconvolution, the largest standard deviations of other quantities, such as the total-field anomaly or its horizontal derivatives, fail in interpreting interfering or elongated anomalies, whereas the vertical derivative of the total-field anomaly is more robust.

For a visual convenience, let us consider the kth and $(k+1)$th moving-data windows located over a geologic source. Fig. 1a shows a schematic pictorial representation of the classic plot of Euler estimates from a total-field anomaly with vertical magnetization assuming the correct SI, where the red rectangle outlines the horizontal projections of the source. In this plot, the kth and $(k+1)$th estimates are shown such as displayed in Reid et al. (1990). In this plot, the estimates of the horizontal coordinates $\widehat{x}_o$ and $\widehat{y}_o$ are plotted on the $x-y$ plane, and the depth estimate $\widehat{z}_o$ is plotted using color depth scale. Specifically, we are using colored circles to locate the estimates. Over the source and assuming the correct SI the horizontal and vertical estimates have values that are very close to the true source coordinates producing therefore the tightest cluster of source-position estimates. Usually the estimates $\widehat{b}$ are neglected, although they are calculated in Eq. (3). Here, the base-level estimates are plotted in the same way as depth estimates shown in Fig. 1a. Fig. 1b shows the base-level estimates $\widehat{b}$ for the correct SI in the same estimates of horizontal coordinates (shown Fig. 1a) and using a color scale in nanotesla.
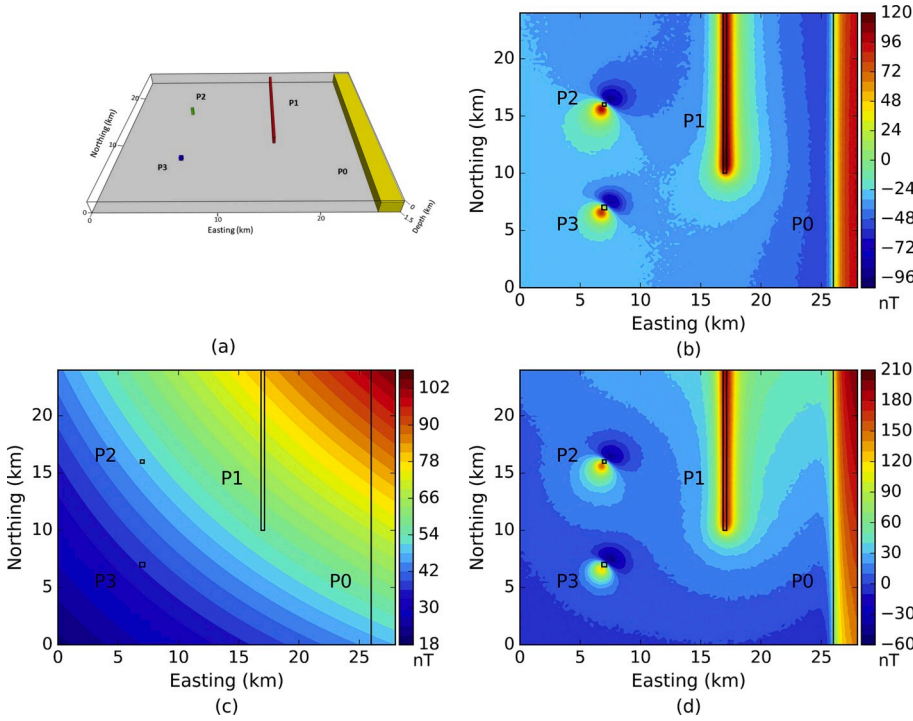
We compared our methodology to select reliable Euler solutions with two discrimination techniques described in FitzGerald et al. (2004). With these techniques, we reject the Euler estimates based on: i) the rejection of the moving-data windows where the signal strength of the total-field anomaly is less than some specified threshold; and ii) the rejection of the estimates whose the ratio of the depth uncertainty and the estimated depth is greater than a percentage. The criterion to define the threshold of the strength of the anomaly is to have moving-data windows over the positive and negative sides of the anomaly, when available. The criterion to define the percentage of ratio of the depth uncertainty and the estimated depth (henceforth referred to depth uncertainty) is to have a minimum number of Euler estimates over the anomalies. We used both discrimination techniques in sequence, i.e., we reject Euler estimates where the center of the moving-data window is below a specified threshold of the signal strength and then we reject a percentage of the remaining estimates which have the depth uncertainty greater than a defined value.

4. Results

4.1. Synthetic test 1 – distinct SIs and strong nonlinear magnetic base level

Fig. 2a shows four prisms that represent the sources of the simulated total-field anomaly in Fig. 2b. The prisms labelled P0–P3 in Fig. 2a simulate geological sources with distinct SIs. The prism P0 which simulates a contact has SI = 0, top at 0.2 km and magnetization intensity of 0.3 A/m. The prism P1 simulates a thin dike which has SI = 1, top at 0.6 km, 0.4 km width and magnetization intensity of 2 A/m. The prism P2 which simulates a vertical intrusion has SI = 2, top at 0.6 km, equal horizontal dimensions of 0.3 km and magnetization intensity of 15 A/m. Finally, the prism P3 simulates a spherical source which has SI = 3, radius of 0.2 km, center at 1.050 km and magnetization intensity of 25 A/m. The main field has inclination of 70° and declination of −20°, the sources P0 and P1 have induced magnetization and the sources P2 and P3 have remanent magnetization with inclination of 20° and declination of 40°. We simulated a survey on a regular grid of 120×140 observation points in the x- and y-directions equally spaced at each 0.2 km and the survey height is simulated at $z = -0.1$ km. Fig. 2b shows the simulated total-field anomaly (Uieda et al., 2013) corrupted with pseudorandom Gaussian noise with zero mean and standard deviation of 0.5% of the maxima absolute amplitude of the data (0.6 nT). The generated noise (not shown) have amplitude ranging from −2.25 nT to 2.13 nT. Fig. 2c shows a simulated nonlinear background generated by the polynomial:

Fig. 1. Schematic pictorial representation of the classic plot of Euler deconvolution estimates for the correct SI over a source, outlined by a red rectangle. The kth and $(k + 1)$th horizontal coordinate estimates show $\widehat{x}_o^k$ and $\widehat{y}_o^k$ plotted at its plan (x, y) position, (a) $\widehat{z}_o$ and (b) $\widehat{b}$ are plotted using colored circles according to their color bars. (For interpretation of the references to color in this figure legend, the reader is referred to the Web version of this article.)

Fig. 2. Synthetic test 1: Simulated sources and magnetic anomaly. (a) Simulated sources P0–P3 represent a contact (SI = 0), a dike (SI = 1), a vertical intrusion (SI = 2) and a spherical source (SI = 3), respectively. (b) Noise-corrupted total-field anomaly (the noise standard deviation is 0.6 nT) generated by the sources shown in panel a. (c) Nonlinear base level simulating a regional field. (d) Noise-corrupted magnetic anomaly obtained by adding the total-field anomaly shown in panel b to the nonlinear base level shown in c. The black polygons in panels b–d outline the horizontal projections of the simulated sources shown in panel a.

$$b(x_j, y_j) = \frac{(x_j + 20)(y_j + 20)}{20}, \qquad (5)$$

where the subscript j is related to the jth observation point (x_j, y_j). As pointed in Melo and Barbosa (2018), this anomaly can simulate a regional field, a strongly interfering anomaly, or a poor definition of the IGRF. Notice that this base level has values of amplitudes higher than the anomalies in Fig. 2b, thus generating strongly interfering anomalies after its addition to the original data (Fig. 2b). Fig. 2d shows the noise corrupted magnetic anomaly generated by the addition of the total-field anomaly in Fig. 2b with the nonlinear base level in Fig. 2c. Notice in Fig. 2d that the superposition effect due to the addition of the simulated nonlinear base level (Fig. 2c) yields a strong interference in the original anomaly shown in Fig. 2b. Therefore, the generated data (Fig. 2d) no longer have the same amplitude and shape of the original data (Fig. 2b). In fact, at some locations the amplitude of the magnetic data yielded by the nonlinear base level is greater than twice the original anomaly (Fig. 2b) generating strongly interfering anomalies (Fig. 2d). The black polygons in Fig. 2b–d outline the horizontal projections of the simulated sources shown in perspective view in Fig. 2a.

Fig. 3a shows the vertical derivative of the total-field anomaly

(Fig. 2d) and the projection of the sources in thin black polygons. We run Euler deconvolution using the magnetic data shown in Fig. 2d with a moving-data window of 7 × 7 points solving Eq. (3) for each position of the moving-data window. Fig. 3b shows all the Euler deconvolution source-position estimates. Fig. 3c shows the standard deviation of the vertical derivatives of the total field anomaly computed on a moving-data window of 7 × 7 points. In Fig. 3c, the thick black lines encompass the 10% of the moving-data windows with the largest standard deviations of the vertical derivatives of the magnetic data. Hence, our methodology defines areas (Fig. 3c) that enclose the magnetic anomalies and these areas are larger than the areas (not depicted) formed by the high values in the vertical derivative (Fig. 3a) such as the edges of the sources P0 and P1. By applying the Euler deconvolution to the interfering synthetic magnetic data shown in Fig. 2d, we will estimate the depths to the tops of the sources P0–P2 and the depth to center of the source P3 (Reid and Thurston, 2014).

Fig. 4 shows the results of the proposed methodology where the horizontal position estimates (in circles) of the sources are displayed over the map of the magnetic anomaly (in grayscale) and the depth estimates are represented by distinct colors. Fig. 4a–d shows the Euler estimates assuming the SI = 0, 1, 2 and 3, respectively. The tightest
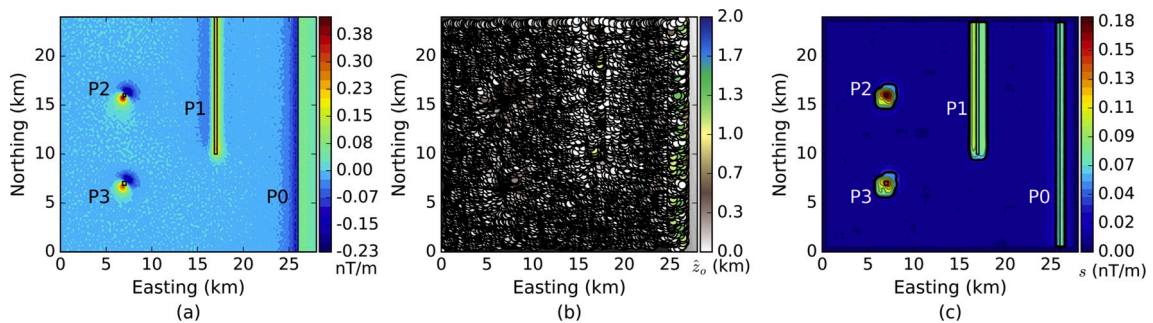

Fig. 3. Synthetic test 1: Vertical derivative, Euler solutions and standard deviation of the derivative. (a) Vertical derivative of the total-field anomaly (Fig. 2d). (b) All Euler deconvolution source-position estimates. (c) Standard deviation of the vertical derivative of the total-field anomaly computed on a moving-data window of 7 × 7 points. The grey contour lines are plotted every 0.02 nT/m and the limit to accept solutions is delineated by the thick black lines and encloses the 10% of the largest standard deviations.
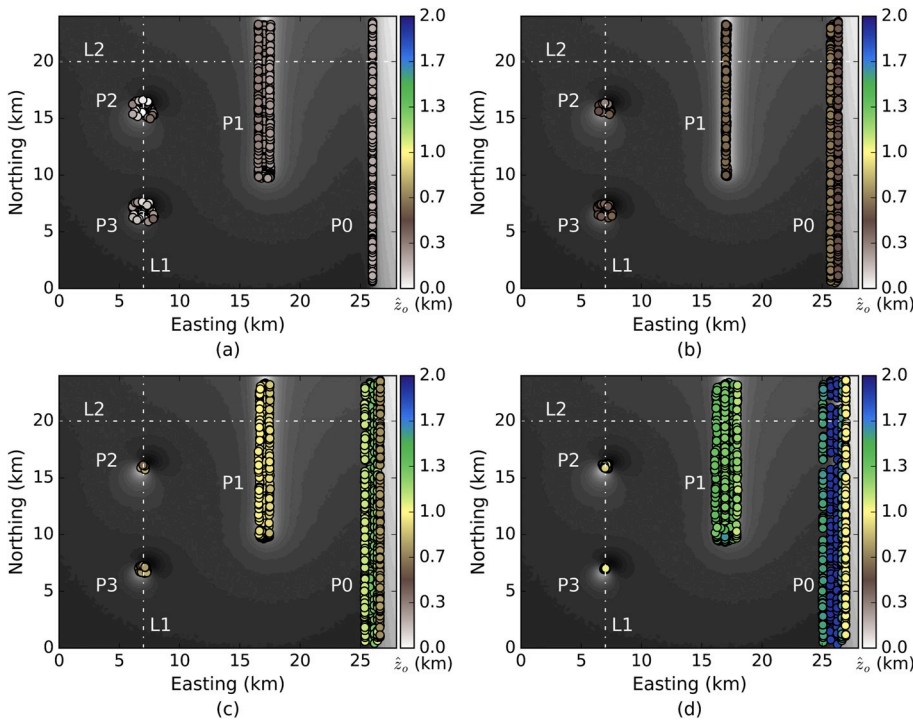
Fig. 4. Synthetic test 1: Reliable Euler deconvolution source-position estimates (colored circles) with the proposed methodology over the total-field anomaly (grayscale). Source-position estimates assuming (a) SI = 0 (b) SI = 1, (c) SI = 2 and (d) SI = 3. The selected Euler estimates are the ones that are obtained by using the data windows with the largest standard deviations (areas in Fig. 3c) of the vertical derivatives of the total-field anomaly. Euler deconvolution estimates are shown in Fig. 6a and b over the profiles L1 and L2 (dashed white lines).

cluster of the estimates over the source P0 in Fig. 4a defines the depth to the top of the contact at 0.201 km. Fig. 4b shows tightest cluster of the source-position estimates assuming the SI = 1, the correct one for the source P1. In this cluster of estimates, the mean of the depth estimates is 0.618 km, which is very close to the depth to the top of the simulated thin dike P1. In Fig. 4c, the tightest cluster of the estimates is over the source P2 because we assume the SI = 2. The mean of the depth estimates in this cluster defines the depth to the top of the vertical intrusion at 0.634 km. In this test, the amplitude of the magnetic anomaly due to source P2 (vertical intrusion) is the smallest one; however, our methodology was able to retrieve the depth of the top of the source P2 correctly. Finally, Fig. 4d shows the tightest cluster of the source-position estimates over the source P3 by assuming the SI = 3. The mean of depth estimates over this source retrieves the depth to the
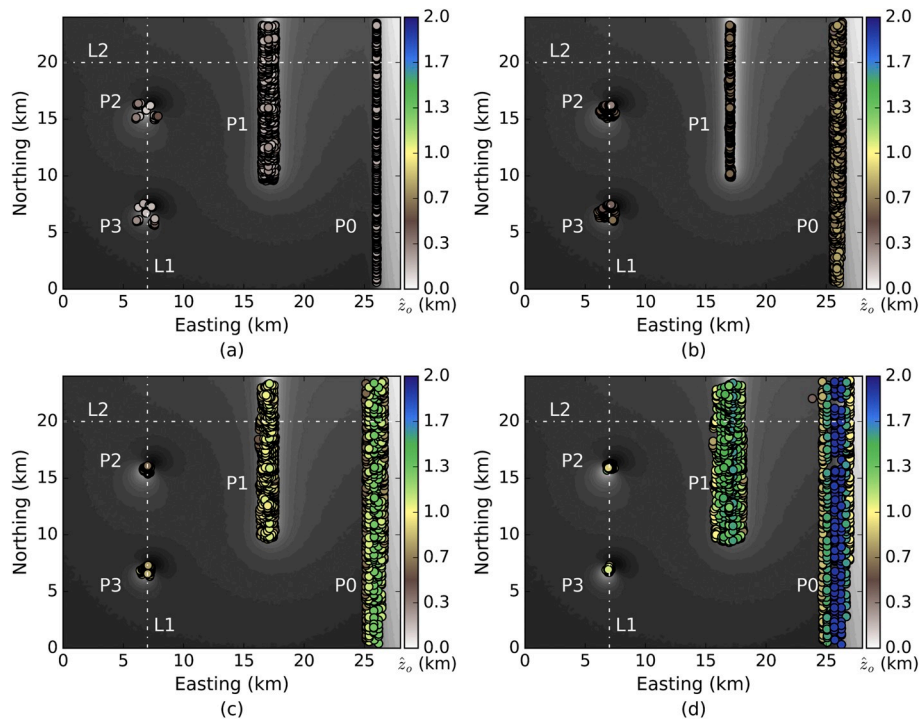
Fig. 5. Synthetic test 1: Reliable Euler deconvolution source-position estimates (colored circles) with two other methodologies over the total-field anomaly (grayscale). Source-position estimates assuming (a) SI = 0 (b) SI = 1, (c) SI = 2 and (d) SI = 3. The selected Euler estimates are the ones obtained by the rejection criteria based on the amplitude of the data and on depth uncertainty. Euler deconvolution estimates are shown in Fig. 6c and d over the profiles L1 and L2.

center of the spherical source at 1.055 km. In the following, Euler deconvolution estimates will be shown over the profiles L1 and L2.

For comparison, we show in Fig. 5 the reliable Euler deconvolution estimates selected by means of two discrimination techniques described in FitzGerald et al. (2004). First, we run Euler deconvolution and defined a threshold to reject solutions where the moving-data window center pass over an anomaly of ±20 nT. Second, we reject the remaining solutions that have a depth uncertainty greater than 20%. Then, the selected estimates are plotted on Fig. 5a–d assuming the SI 0, 1, 2 and 3, respectively. Based on the clustering of solutions, the sources P0, P1 and P3 are identified by the correct assumption of the SIs 0, 1 and 3 in Fig. 5a, b and 5d, respectively. However, the nature of the source P2 is not clearly identifiable from the SI equal to 2 (Fig. 5c) or SI equal to 3 (Fig. 5d).

Fig. 6a and b shows the profiles L1 and L2 from the estimates computed with the proposed methodology (Fig. 4). The black arrows point to the correct depth of the sources. Notice that the reliable Euler estimates by using our method (Fig. 6a and b) are clustered on the correct depth position. Fig. 6c and d shows the profiles L1 and L2 from the estimates computed with the rejection criteria based on the amplitude of the data and on depth uncertainty (Fig. 5). The black arrows point to the correct depth of the sources. Notice in Fig. 6c that the estimates from SIs equal to 3 (stars) and 2 (green dots) are clearly scattered in depth, although the estimates from SI equal to 3 are clustered on the plan view of Fig. 5d (source P3). In Fig. 6d, the estimates from SI equal to 1 (red triangles) and 0 (blue dots) are reasonably clustered over the correct depths.

Fig. 7 shows the results of the proposed methodology where the base-level estimates (shown in colored circles) are displayed over the map of the magnetic anomaly (Fig. 2d), shown in grayscale. Fig. 7a–d shows the estimates assuming the SI = 0, 1, 2 and 3, respectively. As written in Melo and Barbosa (2018), the base-level estimates in Fig. 7a have the amplitude amplified because the SI is zero. As in the source-position estimates shown in Fig. 4, the tightest cluster of base-level estimates defines the correct SI.

The definition of the correct SI in the results shown in Figs. 4, 6 and 7 is possible because of the tightest clustering of the source-position and base-level estimates. The nonlinear base level does not affect the proposed methodology because we select the reliable Euler deconvolution estimates throughout the moving-data windows with the largest

standard deviations of the vertical derivatives of the data (Fig. 3c). Thus, we selected only the moving-data windows where a factual source is present. The selection of reliable Euler solutions from the combination of two classic methodologies could not define the correct SI such as shown in Fig. 6c.

4.2. Synthetic test 2 – anomalies with distinct amplitudes

Fig. 8a shows the total-field anomaly generated by four prisms that resemble spherical sources. The prism P0 has width of 0.8 km, is centered at 1 km deep and has magnetization intensity of 1 A/m. The prism P1 has width of 0.6 km, is centered at 0.9 km deep and has magnetization intensity of 1.5 A/m. The prism P2 has width of 0.4 km, is centered at 0.7 km deep and has magnetization intensity of 1.5 A/m. Finally, the prism P3 has width of 0.2 km, is centered at 0.5 km deep and has magnetization intensity of 3 A/m. The main field has inclination of 70° and declination of −20° and the sources have remanent magnetization with inclination of 20° and declination of 40°. We simulated a survey on a regular grid of 25 × 60 observations, with a grid spacing of 0.2 km in both x- and y-directions, at a constant survey height of 0.1 km. The simulated total-field anomaly is corrupted with pseudorandom Gaussian noise with zero mean and a standard deviation of 0.5% of the maxima absolute amplitude of the data (0.2 nT). The generated noise (not shown) have amplitude ranging from −0.77 nT to 0.67 nT. Notice in Fig. 8a that the anomalies generated by the sources P0–P2 interfere on each other.

We run Euler deconvolution using the noise-corrupted total-field anomaly shown in Fig. 8a with a moving-data window of 7 × 7 points. Fig. 8b shows the standard deviation of the vertical derivatives of the total-field anomaly. The thick black lines encompass the 24% of the moving-data windows with the largest standard deviations of the vertical derivatives of the magnetic data.

Fig. 9a shows the reliable Euler estimates, by assuming the SI equal to 3, displayed over the map of the noisy total-field anomaly (in grayscale) and computed from the proposed methodology. We note that the estimates of the horizontal positions of the sources P0–P3 form tight clusters (Fig. 9a). Regarding the depth estimates, the means of the clusters of these estimates over the sources P0–P3 defined the centers at, respectively, 1.045 km, 0.931 km, 0.723 km and 0.482 km deep. These depth estimates are very close to the depths to the centers of the true
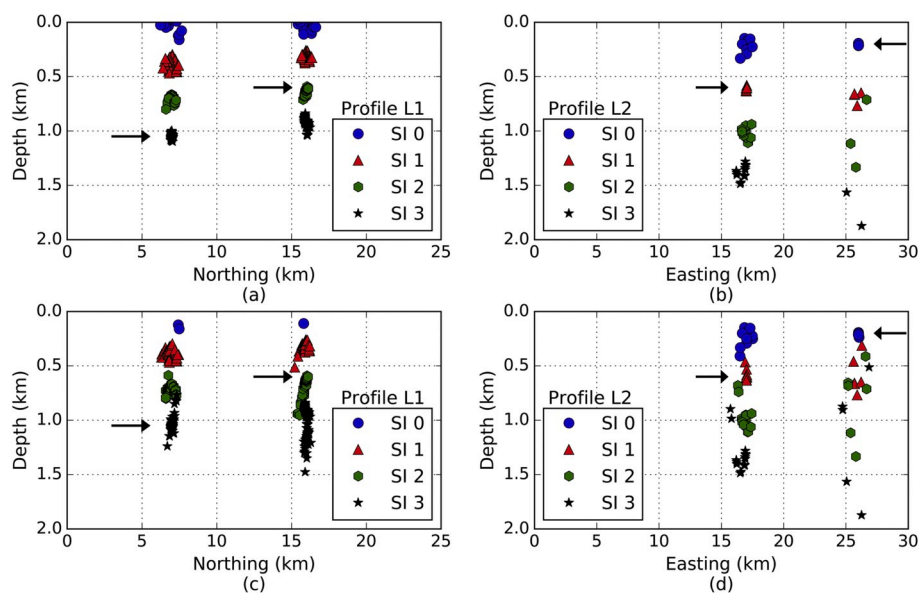

Fig. 6. Synthetic test 1: Profiles over Euler deconvolution source-position estimates. Source-position estimates of Fig. 4, defined with the proposed methodology: (a) Profile L1 over anomalies P3 and P2, and (b) Profile L2 over anomalies P1 and P0. Source-position estimates of Fig. 5, defined with two other methodologies: (c) Profile L1 over anomalies P3 and P2, and (d) Profile L2 over anomalies P1 and P0. The arrows point to the correct depth position of the sources.
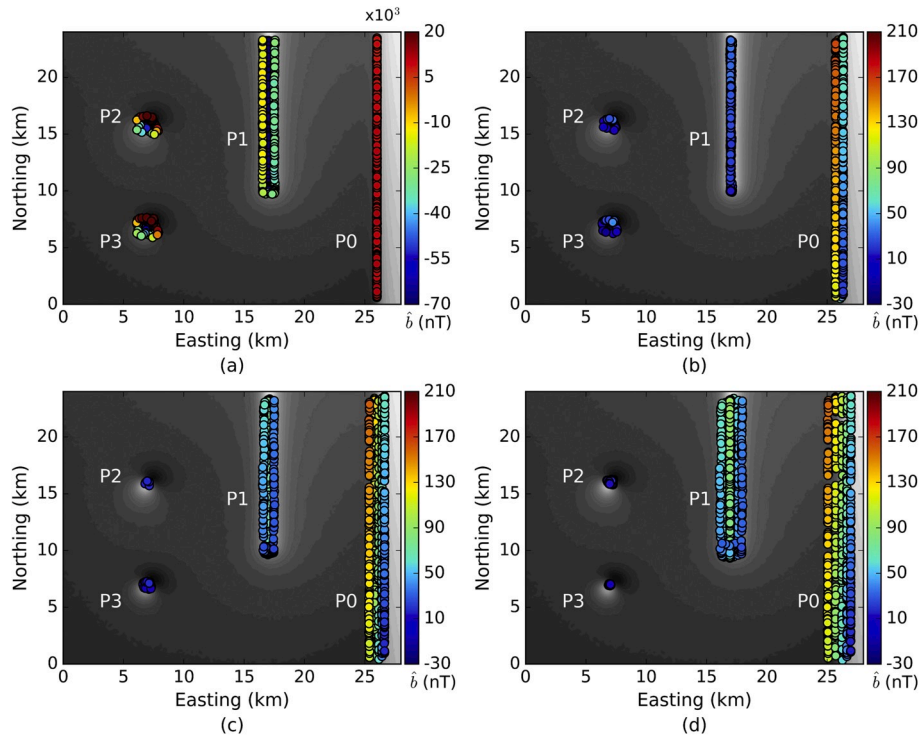
Fig. 7. Synthetic test 1: Euler deconvolution base-level estimates (colored circles) over the total-field anomaly (grayscale). Base-level estimates assuming (a) SI = 0 (b) SI = 1, (c) SI = 2 and (d) SI = 3. The selected Euler estimates are the ones that are obtained by using the data windows with the largest standard deviations of the vertical derivatives of the total-field anomaly.
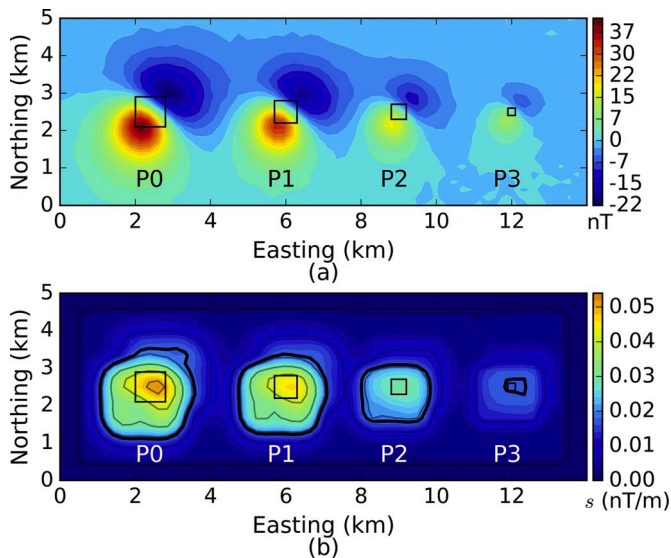
Fig. 8. Synthetic test 2: Total field anomaly and standard deviation of the vertical derivative. (a) Noise-corrupted total-field anomaly produced by sources P0–P3 outlined by black squares. The true centers of the sources P0–P3 are, respectively, at 1 km, 0.9 km, 0.7 km and 0.5 km deep. (b) Standard deviation of the vertical derivative of the total-field anomaly computed on a moving-data window of 7×7 points. In panel b the grey contour lines are plotted every 0.01 nT/m and the limit to accept solutions is delineated by the thick black lines and encloses 24% of the largest standard deviations.

sources P0–P3, which are, respectively, 1 km, 0.9 km, 0.7 km and 0.5 km.

Fig. 9b shows the reliable Euler estimates, by assuming the SI equal to 3, displayed over the map of the noisy total-field anomaly (in gray-scale) and computed from the rejection criteria of the amplitude and depth uncertainty. The threshold to reject amplitudes is ±5 nT and from these estimates the ones with depth uncertainties larger than 20% were rejected. In contrast with our result (Fig. 9a), the estimates of the horizontal positions of the sources P0–P3 are scattered (Fig. 9b) due to the interfering anomalies. Similarly to our result (Fig. 9a), the means of the clusters of the depth estimates over the sources P0–P3 are very close to the depths to the centers of the true sources. These depth estimates of the sources P0–P3 are 1.032 km, 0.927 km, 0.689 km and 0.488 km, respectively.

Fig. 9c shows the profile (dashed white line on Fig. 9a and b) of the reliable Euler estimates computed with our methodology (s) and with the combination of the rejection criteria from amplitude and depth uncertainty ($A + \delta z$). The arrows point to the correct depth position of the sources P0–P3. In this profile, we notice that the reliable Euler solutions defined by our methodology (red stars in Fig. 9c) form tight clustering either in depth estimates or in horizontal estimates of the sources. Rather, the reliable Euler solutions defined by the combination of the rejection criteria from amplitude and depth uncertainty (blue dots in Fig. 9c) generate a spray of solutions.

4.3. Synthetic test 3 – interfering anomalies

In this test, we simulate the total-filed anomaly (Fig. 10) generated by two sources and compute the Euler deconvolution to test the sensitivity of the proposed method to interfering anomalies. This test was inspired by a sensitivity tested shown in Melo et al. (2013). The source P1 is an elongated prism in depth and in the east direction simulating a dike with SI equal to 1, with top at 1 km, width of 0.3 km and the edge located at $y = 8$ km. The source P3 is a prism with equal dimensions of 0.4 km simulating a sphere with SI equal to 3 and centered at 1 km deep. In this test, the source P1 will be keep in the same place and the source P3 will be displaced toward the direction of the source P1 (east direction). The induced field has vertical magnetization. We calculate the total-field anomaly at the ground level on a regular grid of 50×65 observation points in the north–south and east–west directions with grid
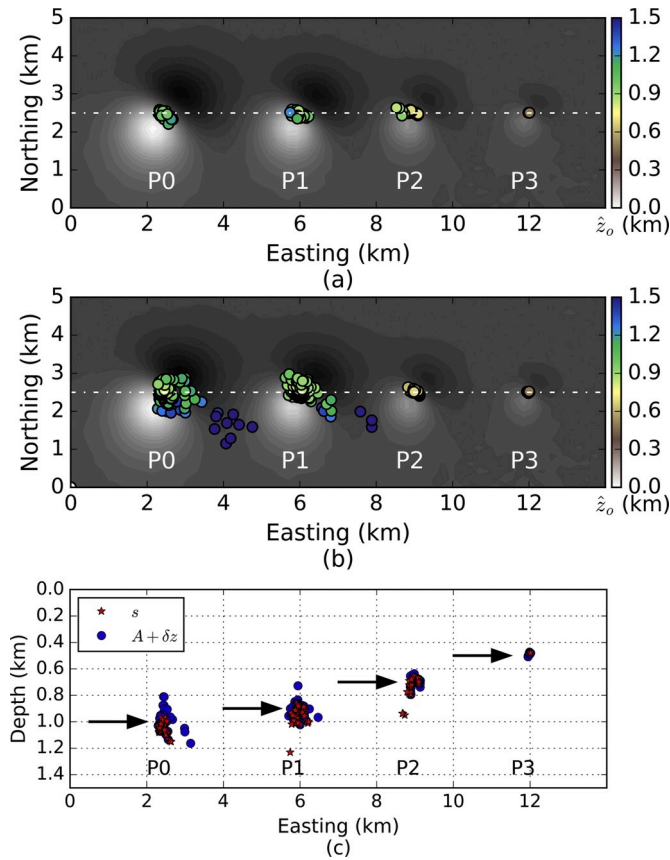
Fig. 9. Synthetic test 2: Reliable Euler deconvolution estimates assuming SI equal to 3. (a) Estimates obtained by our methodology. (b) Estimates obtained by the combination of the rejection criteria from amplitude and depth uncertainty. (c) Profile with the reliable Euler estimates by our methodology (s) and by the combination of the rejection criteria from amplitude and depth uncertainty ($A + \delta z$). The arrows point to the correct depth position. The dashed white line in panels a and b establishes the location of the profile shown in panel c.

spacing of 0.2 km along both directions. The pseudorandom Gaussian noise added to the data has zero mean with standard deviation of (0.12 nT), reaching an amplitude range of ±0.48 nT. Fig. 10a shows the noisy total-field anomaly where the source P3 is centered at $y_o = 4$ km establishing a distance from the source P1 of $\Delta y = 4$ km. Fig. 10b, c and 10d show the noisy total-field anomalies where the source P3 are centered, respectively, at $y_o = 6$ km, $y_o = 7$ km and $y_o = 7.5$ km establishing distances from the source P1, respectively, of $\Delta y = 2$ km, $\Delta y = 1$ km and $\Delta y = 0.5$ km. Notice that these distances (Δy) are not lengths that were measured the borders of the sources; actually, they are the distances between the positions that are estimated by Euler deconvolution, i.e., the center of the source P3 and the edge of the source P1. We call attention in Fig. 10d that the distance between the borders of the sources is 0.3 km whereas $\Delta y = 0.5$ km and with a visual inspection is not possible to observe if the anomaly is generated by one or more sources.

To select reliable Euler solutions by using our methodology, we applied Euler deconvolution to the data shown in Fig. 10a ($\Delta y = 4$ km) and 10 b ($\Delta y = 2$ km) using a moving-data window of 7 × 7 points and selecting 7% of the solutions. To the data shown in Fig. 10c ($\Delta y = 1$ km), we used a moving-data window of 5 × 5 points and selecting 4% of the solutions. Finally, we used a moving-data window of 3 × 3 points and selecting 3% of the solutions to the data shown in Fig. 10d ($\Delta y = 0.5$ km). Fig. 11 shows the profile (see location in Fig. 10) of the reliable Euler estimates by using the correct SIs (i.e., SI = 1 to the source P1 and SI = 3 to the source P3). Fig. 11a shows the reliable Euler estimates

obtained by our methodology and Fig. 11b shows the reliable estimates obtained by the combination of the rejection criteria from amplitude and depth uncertainty. The threshold to reject amplitudes is ±20 nT and from these estimates the ones with depth uncertainties larger than 15% were rejected. Notice that using both criteria the reliable Euler estimates locating the source P3 (SI = 3) are correctly forming clusters at about the east coordinates: 4 km, 6 km, 7 km and 7.5 km. However, by comparing Fig. 11a with Fig. 11b, we can note that the reliable Euler estimates obtained with our method (Fig. 11a) display tighter clusters than the ones shown in Fig. 11b.

4.4. Synthetic test 4 – noisy data

In this test we simulate a total-field anomaly genereted by a vertical prism and compute the Euler deconvolution in order to test the sensitivity of the method to noisy data. The source is a vertical prism elongated in depth, with to top at 0.6 km, width of 0.4 km and magnetization intensity of 10 A/m, the SI of this source is 2. In this test, the induced field has vertical magnetization and the data were computed on the plane $z = 0$ km at the nodes of a 50 × 65 grid with a grid spacing of 0.1 km in the x - and y-directions (north-south and east-west, respectively).

Here, we conduct the sensitivity analysis by perturbing the observations with additive zero-mean Gaussian pseudorandom noise with variable standard deviations that, in turn, are taken as a percentage of the maximum amplitude of the total-field anomaly. The standard deviations are 0.5% (Fig. 12a), 1% (Figs. 12b), 1.5% (Fig. 12c) and 2% (Fig. 12d).

By assuming SI equal to 2, we run Euler deconvolution with a moving-data window of 7 × 7 grid points. For the anomalies shown in Fig. 12a–d, the reliable Euler estimates were obtained by our methodology (Fig. 13a–d) selecting the best 2%, 3%, 6% and 8% of the solutions, respectively. The estimates obtained by the combination of the rejection criteria from amplitude and depth uncertainty (Fig. 13e–h) were selected with the threshold to reject amplitudes of ±100 nT and from these estimates the ones with depth uncertainties larger than 3%, 5%, 10% and 15% were rejected, respectively. Fig. 13 shows that the reliable Euler solutions are clustered over the simulated source for both methods. As expected, the greater the level of the noise (in Fig. 13 from a to d and from e to h), the larger the scattering of the solutions.

Fig. 14 shows the profile (see location in Fig. 13) of the reliable Euler estimates obtained by our methodology (Fig. 14a) and by the combination of the rejection criteria from amplitude and depth uncertainty (Fig. 14b). The reliable Euler estimates with factual noise levels of 0.5% (blue triangles) and of 1% (stars) obtained by both methods display tighter clusters close to the top of the simulated source (0.6 km). For greater noise levels of 1.5% (green circles) and 2% (red crosses), the scattering of the Euler estimates occurs in both methods, as expected. This test shows the well-known sensitive of Euler deconvolution to the presence of high levels of noise (green circles and red crosses in Fig. 14a and b) producing wrong estimates of the source positions and, thus, unreliable solutions.

4.5. Application to real data – Paraná-Santa Catarina project

The aeromagnetic data (yellow polygon in Fig. 15a) were acquired between 2009 and 2011 (CPRM, 2011) over the southeastern and southern Brazil. The acquisition service company processed the new dataset acquired on a modern system with basic routines: parallax correction, diurnal variation correction, leveling of profiles, micro-leveling and removal of IGRF correction. The flight lines in the north–south direction were acquired every 0.5 km, the tie lines were acquired every 10 km and the flight height was approximately constant at $z = -0.1$ km. We gridded the dataset with the algorithm triangulation with linear interpolation, both datasets are gridded every 0.125 km in the x- and y-directions. We study two areas in this survey (yellow polygon in Fig. 15a), namely the Anitápolis anomaly (blue dot in
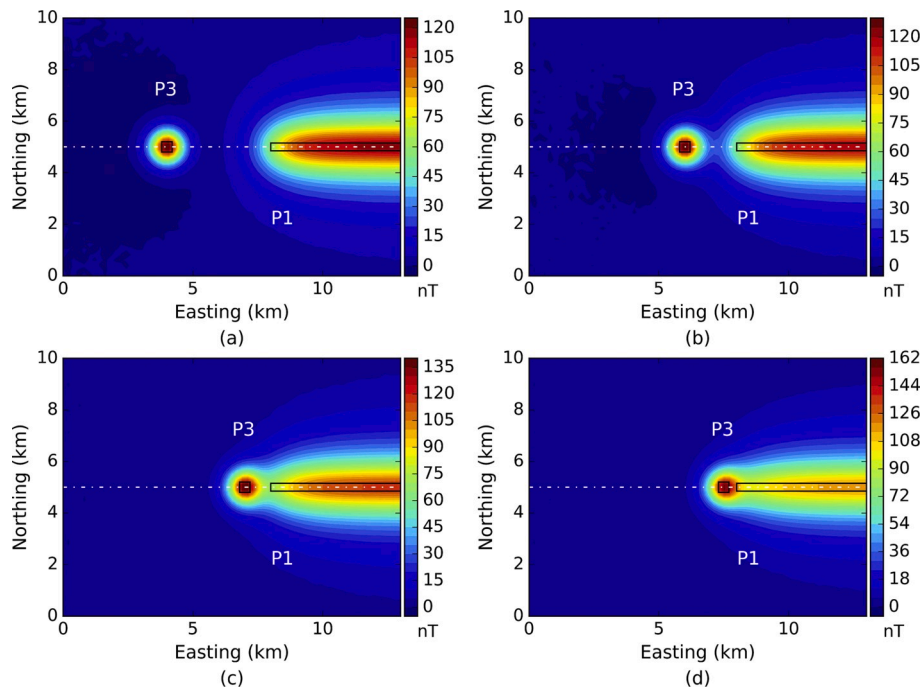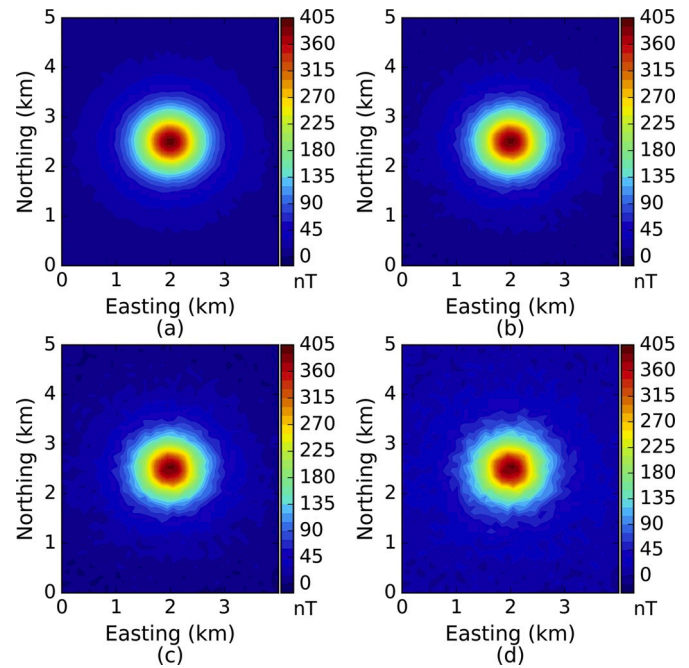
Fig. 10. Synthetic test 3: Interfering anomalies. The distances between the sources P1 to P3 are: (a) $\Delta y = 4$ km, (b) $\Delta y = 2$ km, (c) $\Delta y = 1$ km and (d) $\Delta y = 0.5$ km. The dashed white line in panels a–d establishes the location of the profile shown in Fig. 11.
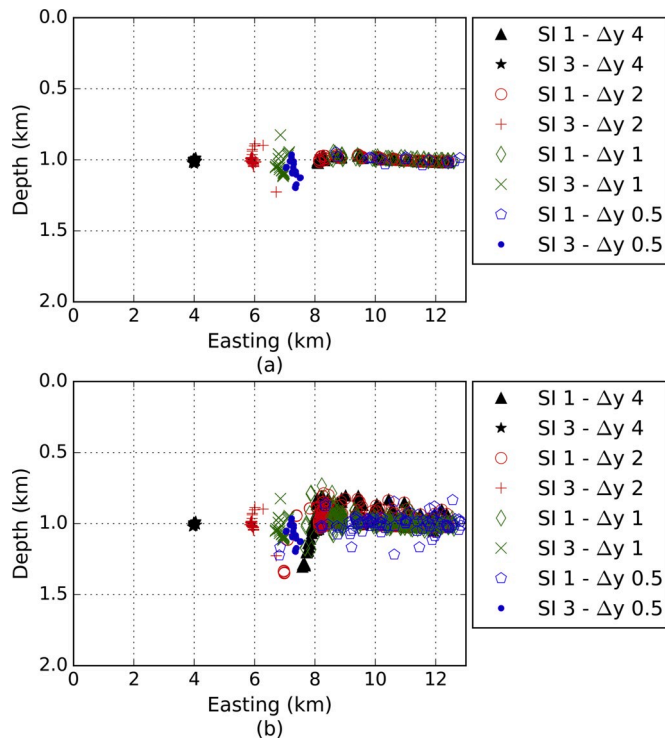
Fig. 11. Synthetic test 3. Profile with the reliable Euler deconvolution estimates assuming the correct SIs to the sources P1 (SI = 1) and P3 (SI = 3). (a) Estimates obtained by our methodology. (b) Estimates obtained by the combination of the rejection criteria from amplitude and depth uncertainty. The correct depths of the sources P1 and P3 are 1 km. The profile is located in Fig. 10.
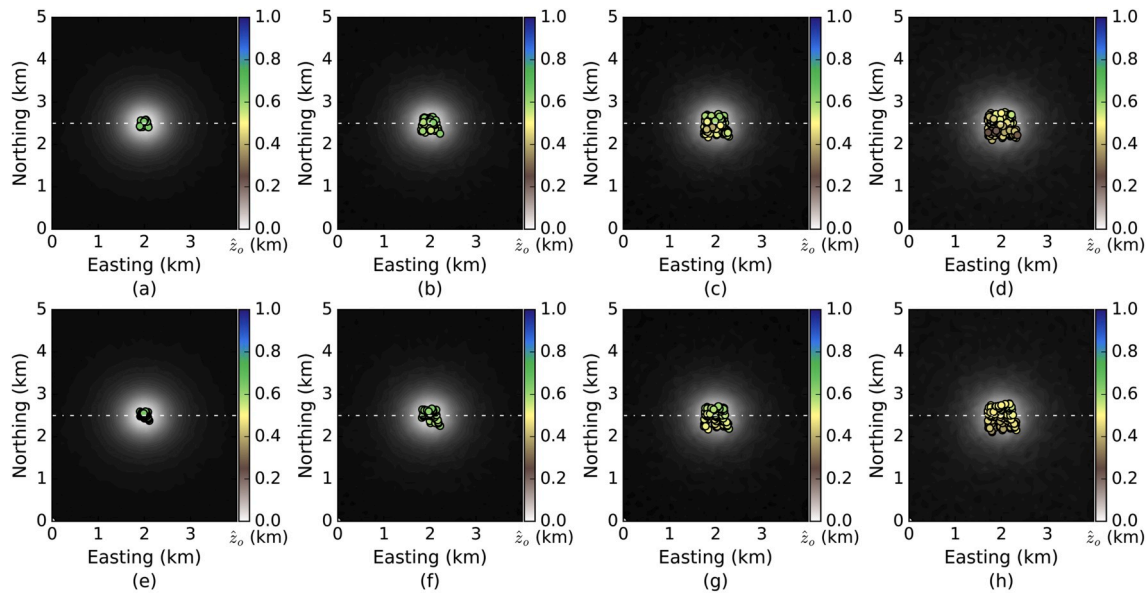

Fig. 12. Synthetic test 4: Noisy total-field anomalies. Total-field anomalies contaminated with additive zero-mean Gaussian pseudorandom noise with standard deviations: (a) 0.5%, (b) 1%, (c) 1.5% and (d) 2% of the maximum amplitude of the anomaly.

Fig. 15a) and the Paranaguá Terrane (green dot in Fig. 15a). Fig. 15b shows the Anitápolis anomaly over the study area, gridded with 145 points northing and 121 points easting; this anomaly is approximately

located at 27.8° south and 49.1° west (WGS84). Fig. 15c shows an area of the Paranaguá Terrane, gridded with 369 points northing and 185 points easting; this area is centralized at 25.8° south and 48.7° west (WGS84).

4.5.1. Anitápolis anomaly

The Santa Catarina state in southern Brazil is characterized by the

Fig. 13. Synthetic test 4. Reliable Euler estimates (colored dots) for anomalies (Fig. 12) contaminated with additive zero-mean Gaussian pseudorandom noise with standard deviations: 0.5%, 1%, 1.5% and 2% of the maximum amplitude of the anomaly. (a)–(d) Estimates obtained by our methodology. (e)–(h) Estimates obtained by the combination of the rejection criteria from amplitude and depth uncertainty. The dashed white line in panels a–h establishes the location of the profile shown in Fig. 14.
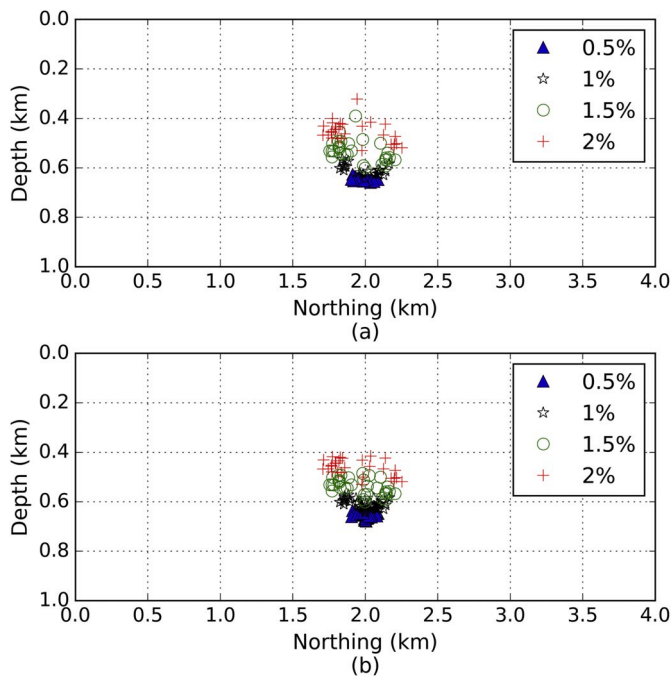
Fig. 14. Synthetic test 4. Profile with the reliable Euler deconvolution estimates for noisy anomalies shown in Fig. 13 with the correct SI = 2, the label shows the percentage of noise. (a) Estimates obtained by our methodology. (b) Estimates obtained by the combination of the rejection criteria from amplitude and depth uncertainty. The correct depths of the source is 0.6 km. The profile is located in Fig. 13.

occurrence of several alkaline and alkaline-carbonatitic bodies of Early to Late Cretaceous age. The Anitápolis alkaline-carbonatite complex (132 Ma) is a small intrusion in the Late Proterozoic Dom Feliciano mobile belt (Scheibe et al., 2005). The complex shows a concentric zonation consisting of phlogopite clinopyroxenites and apatite-biotite-magnetite clinopyroxenites surrounded by ijolites and nepheline syenites that intrude Late Proterozoic granitic-gneissic rocks.

A dyke like carbonatitic core of about ten square meters crops out at the center of the complex in contact with phlogopite clinopyroxenites (Comin-Chiaramonti et al., 2005). The phosphate deposit of Anitápolis produces large amounts of phosphate fertilizers. Apatite is the only mineral worth exploiting economically, and it corresponds to reserves of 206.5 Mt, according to fresh rocks distribution from boreholes (Biondi, 2005). The study area has a near surface well-known geology; however, the shape and the depth of the magnetized source that gives rise to the Anitápolis anomaly are unknown.

We run Euler deconvolution in the data shown in Fig. 15b with a moving-data window size of 7 × 7 grid points. Fig. 16a shows all source-position estimates (unselected solutions), recall that every position of the moving-data window produces a solution solving Eq. (3). Fig. 16b shows the standard deviations of the vertical derivatives of the total-field anomaly (Fig. 15b). The best 0.2% of the solutions are associated with the largest standard deviations and enclosed by the thick black lines in Fig. 16b. Fig. 16c and d shows the source-position estimates obtained by our methodology to define reliable solutions assuming the SI 2 and 3, respectively. Notice that the estimates assuming the SI = 2 (Fig. 16c) yield a tight clustering. Fig. 16e and f shows the source-position estimates obtained by the rejection criteria of amplitude (±500 nT) and depth uncertainty (3%) assuming the SIs equal to 2 and 3, respectively. Fig. 16g shows the base-level estimates obtained by our methodology assuming the SI = 2 because it yields a tight cluster of solutions (Fig. 16c). Fig. 16h shows the source-position estimates from the profile (see location in Fig. 16c–f) of the reliable Euler estimates obtained by: i) our methodology (*s*) shown in Fig. 16c and d, and ii) the rejection criteria of amplitude and depth uncertainty ($A + \delta z$) shown in Fig. 16e and f. By assuming the SI = 2, a single source is clearly seen by the cluster of the solutions obtained by our methodology (green dots) whereas the rejection criteria of amplitude and depth uncertainty clearly yield Euler estimates (red crosses) scattered over larger depth ranges. The mean of the depth estimates from our methodology assuming the SI = 2 is equal to 0.677 km. Recall, that the SI = 2 defines a plug source, so this value defines the depth to the top of a plug intrusion.

4.5.2. Paranaguá Terrane

The Paranaguá Terrane is one of the four geotectonic units of the southern segment of the Ribeira Belt (Heilbron et al., 2010). The study
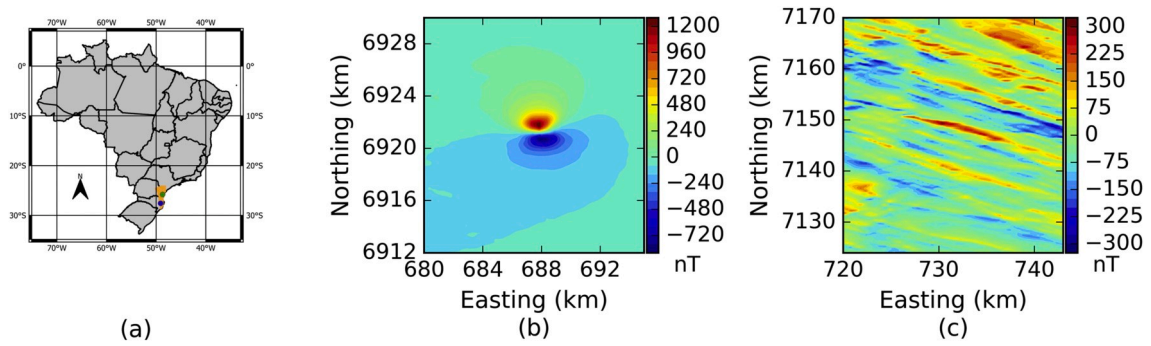
Fig. 15. Real data application: Total field-anomalies. (a) Locations of the aeromagnetic survey (yellow), the Anitápolis anomaly (blue dot) and the Paranaguá Terrae (green dot). (b) Anitápolis total-field anomaly. (c) Total-field anomaly of an area of the Paranaguá Terrane. (For interpretation of the references to color in this figure legend, the reader is referred to the Web version of this article.)
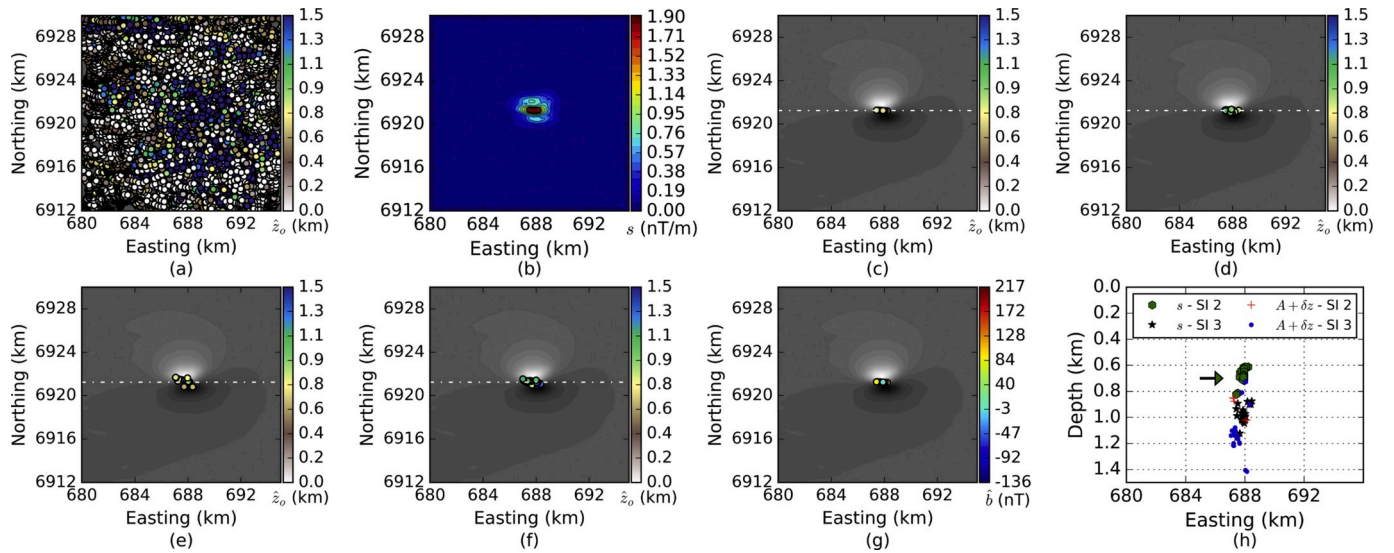
Fig. 16. Anitápolis anomaly, Brazil: Euler deconvolution estimates. (a) All Euler estimates of the source-positions. (b) Standard deviations of the vertical derivatives of the total-field anomaly (Fig. 15b). The thick black line encloses the largest standard deviations defining the best solutions. Reliable Euler source-position estimates from our methodology (s) assuming (c) the SI 2 and (d) the SI 3. Selected Euler source-position estimates from the rejection criteria of amplitude and depth uncertainty ($A + \delta z$) assuming the SI = 2 and (f) the SI = 3. (g) Base-level estimates from our methodology assuming the SI = 2. (h) Profile with the reliable Euler source-position estimates by methods s and $A + \delta z$ with SIs equal to 2 and 3. The dashed white line in panels c–f establishes the location of the profile shown in panel h.

area is characterized by an igneous complex with a variety of granitic rocks on the west, north and east sides, metasedimentary rocks in the central part and quaternary sediments in the south (Cury, 2009; Weihermann et al., 2018). A remarkable feature in the Ribeira Belt is a swarm of dikes with northwest-southeast trend, these magnetic structures reflect a Mesozoic thick swarm of diabase dykes related to the magmatism of the Paraná Basin (Marangoni and Mantovani, 2013; Weihermann et al., 2018).

We run Euler deconvolution in the data shown in Fig. 15c with a moving-data window of 5 × 5 grid points. Fig. 17a shows all source-position estimates (unselected solutions). By assuming the SI equal to 1, we run Euler deconvolution to define the top of the dikes. Fig. 17b shows the standard deviations of the vertical derivatives of the total-field anomaly (Fig. 15c) and the best 13% of the solutions associated with the largest standard deviations limited by the thick black lines. Fig. 17c and d shows the reliable source-position estimates, plotted over the total-field anomaly (grey scale), which were obtained, respectively, by: i) our methodology (s) and ii) the rejection criteria ($A + \delta z$) of amplitude (±75 nT) and depth uncertainty (10%). Both reliable Euler estimates (Fig. 17c and d) display northwest-southeast trends that are also seen in the original total-field anomaly (Fig. 15c). Fig. 17e and f

shows clusters of the reliable source-position estimates (s and $A + \delta z$) over the profiles L1 and L2, respectively. In accordance with Weihermann et al. (2018), these reliable estimates reveal dikes at shallow depths. It is noteworthy that the estimates on Fig. 17c–f appear in both common and distinct locations, i.e., the methods detect the same structures in some locations and in other locations, they detect distinct structures. The complexity of applying Euler deconvolution to this area, with strongly interfering anomalies, shows that both methods (s and $A + \delta z$) to select reliable solutions could be used as complementary tools to aid in the interpretation of Euler deconvolution estimates.

5. Conclusions

We proposed a novel methodology to compute reliable Euler deconvolution estimates. The spray of solutions is reduced selecting the moving-data windows with the largest standard deviations of the vertical derivatives of the total-field anomaly. The tightest cluster of source-position or base-level estimates plotted on the selected moving-data windows with distinct structural indices (SIs) defines the optimum structural index (SI). Finally, we determined the depth of the sources as the mean of the selected depth estimates. The robustness of the
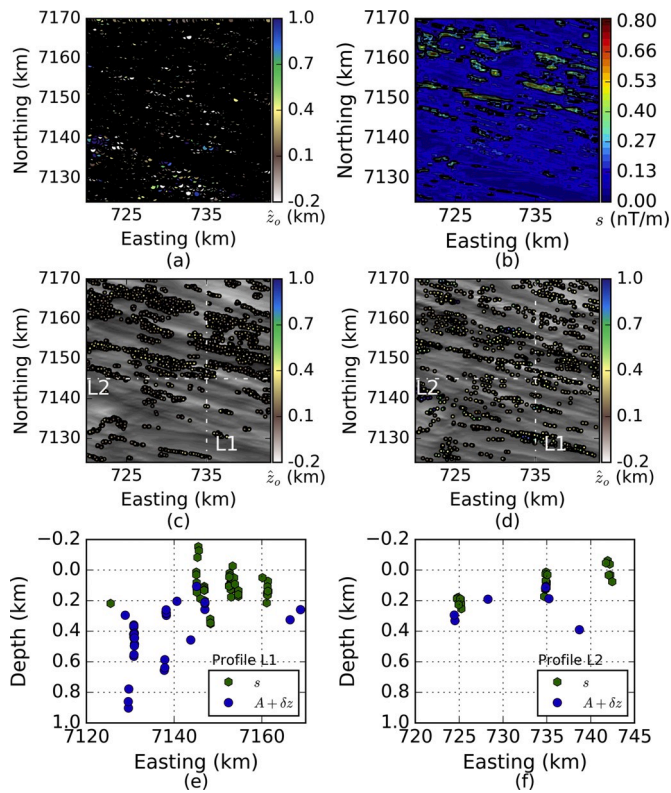
Fig. 17. Paranaguá Terrane anomalies, Brazil: Euler deconvolution estimates. (a) All Euler deconvolution estimates of the source-positions. (b) Standard deviations of the vertical derivative of the total-field anomaly (Fig. 15c). The thick black lines enclose the largest standard deviations defining the best solutions. Selected reliable Euler estimates by assuming SI = 1 obtained by: (c) our methodology (s) and (d) the rejection criteria of amplitude and depth uncertainty ($A + \delta z$). Profiles (e) L1 and (f) L2 with the reliable Euler source-position estimates by our methodology (s) and the rejection criteria ($A + \delta z$). The dashed white lines in panels c and d establish the locations of the profiles L1 and L2 shown in panels e and f.

methodology was proved on synthetic tests where the anomalies were subject to interfering anomalies: i) caused by nonlinear background simulating regional field; ii) with distinct amplitudes and; iii) caused by magnetic sources closely located to each other. As expected, the reliable Euler estimates selected either by our method or by the rejection criteria yielded poor interpretations of high noise levels corrupting the magnetic data. However, the reliable Euler estimates yield sound results in interpreting magnetic data corrupted by realistic levels of noise. Applications to aeromagnetic data from the southern Brazil allowed to infer that: i) an isolated vertical plug intrusion gives rises to the Anitápolis anomaly and ii) a swarm of shallow-seated dikes with northwest-southeast trend gives rise to the complex anomalies over the Paranaguá Terrane. This work is a step further in the selection of reliable estimates in Euler deconvolution and in the understanding of the behavior of the base-level estimates and how they can be used in the determination of the structural index (shape of the magnetic source). Our methodology to define reliable Euler solutions can be used with other discrimination techniques in Euler deconvolution or in any modified versions of Euler deconvolution such as the extended Euler deconvolution. The reliable Euler solutions can be combined in inversion methods to produce a detailed definition of the anomalous sources such as the one that gives rise to the Anitápolis anomaly and the ones that give rise to the complex anomalies over the Paranaguá Terrane.

Data availability

The synthetic magnetic anomaly data is available with the computer code. The Brazilian Geological Survey (CPRM – www.cprm.gov.br) made the real data available.

Computer code availability

All the software used in this paper is open source and was made available in 2019. The synthetic test can be reproduced with the main code euler_python.py and three auxiliary codes. The main algorithm has 9 kb size, was developed in Python and it is compatible with both Python 2.7 and Python 3.7. To run the algorithm, the library numpy is necessary and, in addition, to run the synthetic test the library matplotlib is necessary. The package with instructions is available at: https://github.com/ffigura/Euler-deconvolution-python. The main developer is Felipe F. Melo (email: felipe146@hotmail.com, phone: +5521997270048).

Declaration of competing interests

The authors declare that they have no known competing financial interests or personal relationships that could have appeared to influence the work reported in this paper.

CRediT authorship contribution statement

Felipe F. Melo: Methodology, Writing - original draft. **Valéria C.F. Barbosa:** Supervision, Writing - original draft.

Appendix A. Supplementary data

Supplementary data to this article can be found online at https://doi.org/10.1016/j.cageo.2020.104436.

References

Barbosa, V.C.F., Silva, J.B.C., 2011. Reconstruction of geologic bodies in depth associated with a sedimentary basin using gravity and magnetic data. Geophys. Prospect. 59, 1021–1034.

Barbosa, V.C.F., Silva, J.B.C., Medeiros, W.E., 1999. Stability analysis and improvement of structural index estimation in Euler deconvolution. Geophysics 64, 48–60.

Beiki, M., Pedersen, L.B., 2010. Eigenvector analysis of gravity gradient tensor to locate geologic bodies. Geophysics 75 (6), I37.

Biondi, J.C., 2005. Brazilian mineral deposits associated with alkaline and alkaline-carbonatite complexes. In: Comin-Chiaramonti, P., Gomes, C.B. (Eds.), Mesozoic to Cenozoic Alkaline Magmatism in the Brazilian Platform. Edusp/Fapesp, São Paulo, pp. 707–750.

Blakely, R.J., 1996. Potential Theory in Gravity and Magnetic Applications. Cambridge University Press, New York, NY, USA, p. 441.

Comin-Chiaramonti, P., Gomes, C.B., Censi, P., Speziale, S., 2005. Carbonatites from southeastern Brazil: a model for the carbon and oxygen isotope. In: Comin-Chiaramonti, P., Gomes, C.B. (Eds.), Mesozoic to Cenozoic Alkaline Magmatism in the Brazilian Platform. Edusp/Fapesp, São Paulo, pp. 629–656.

Cooper, G.R.J., 2006. Obtaining dip and susceptibility information from Euler deconvolution using the Hough transform. Comput. Geosci. 32 (10), 1592–1599.

CPRM, 2011. Project: Aerogeophysical survey Paraná-Santa Catarina: Survey and data processing: Final report, Rio de Janeiro, Brazil, 22 (and maps [in Portuguese]).

Cury, L.F., 2009. Geologia do Terreno Paranaguá. (Tese de Doutorado). Instituto de Geociências, Universidade de São Paulo, (São Paulo), p. 202 (p. In Portuguese)).

Durrheim, R.J., Cooper, G.R.J., 1998. EULDEP: a program for the Euler deconvolution of magnetic and gravity data. Comput. Geosci. 24 (6), 545–550.

Fairhead, J.D., Bennett, K.J., Gordon, D.R.H., Huang, D., 1994. Euler: beyond the "Black Box": 64th Annual International Meeting. SEG, Expanded Abstracts, pp. 422–424.

Fedi, M., Florio, G.F., 2003. Decorrugation and removal of directional trends of magnetic fields by the wavelet transform: application to archaeological areas. Geophys. Prospect. 51, 261–272.

FitzGerald, D., Reid, A.B., McInerney, P., 2004. New discrimination techniques for Euler deconvolution. Comput. Geosci. 30, 461–469.

Florio, G., Fedi, M., Pasteka, R., 2014. On the estimation of the structural index from low-pass filtered magnetic data. Geophysics 79 (6), J67–J80.

Gerovska, D., Araúzo-Bravo, M.J., 2003. Automatic interpretation of magnetic data based on Euler deconvolution with unprescribed structural index. Comput. Geosci. 29 (8), 949–960.

Gubbins, D., 2004. Time Series Analysis and Inverse Theory for Geophysicists. Cambridge University Press, New York, NY, USA, p. 272.

Heilbron, M., Duarte, B.P., Valeriano, C.M., Simonetti, A., Machado, N., Nogueira, J.R., 2010. Evolution of reworked Paleoproterozoic basement rocks within the Ribeira belt (Neoproterozoic), SE-Brazil, based on U/Pb geochronology: implications for paleogeographic reconstructions of the São Francisco-Congo paleocontinent. Precambrian Res. 178, 136–148.

Jacobsen, B., 1987. A case for upward continuation as a standard separation filter for potential-field maps. Geophysics 52, 1138–1148.

Leblanc, G.E., Morris, W.A., 2001. Denoising of aeromagnetic data via the wavelet transform. Geophysics 66 (6), 1793–1804.

Marangoni, Y.R., Mantovani, M.S.M., 2013. Geophysical signatures of the alkaline intrusions bordering the Paraná Basin. J. S. Am. Earth Sci. 41, 83–98.

Mauring, E., Kihle, O., 2006. Leveling aerogeophysical data using a moving differential median filter. Geophysics 71, L5–L11.

Melo, F.F., Barbosa, V.C.F., Uieda, L., Oliveira Jr., V.C., Silva, J.B.C., 2013. Estimating the nature and the horizontal and vertical positions of 3D magnetic sources using Euler deconvolution. Geophysics 78 (6), J87–J98.

Melo, F.F., Barbosa, V.C.F., 2018. Correct structural index in Euler deconvolution via base-level estimates. Geophysics 83 (6), J87–J98.

Mikhailov, V., Galdeano, A., Diament, M., Gvishiani, A., Agayan, S., Bogoutdinov, S., Graeva, E., Sailhac, P., 2003. Application of artificial intelligence for Euler solutions clustering. Geophysics 68, 168–180.

Minty, B.R.S., 1991. Simple microlevelling for aeromagnetic data. Explor. Geophys. 22, 591–592.

Mushayandebvu, M.F., van Driel, P., Reid, A.B., Fairhead, J.D., 2001. Magnetic source parameters of two-dimensional structures using extended Euler deconvolution. Geophysics 66, 814–823.

Nabighian, M.N., Hansen, R.O., 2001. Unification of Euler and Werner deconvolution in three dimensions via the generalized Hilbert transform. Geophysics 66, 1805–1810.

Pašteka, R., Richter, F.P., Karcol, R., Brazda, K., Hajach, M., 2009. Regularized derivatives of potential fields and their role in semi-automated interpretation methods. Geophys. Prospect. 57, 507–516.

Reid, A.B., Allsop, J.M., Granser, H., Millett, A.J., Somerton, I.W., 1990. Magnetic interpretation in three dimensions using Euler deconvolution. Geophysics 55, 80–91.

Reid, A.B., Ebbing, J., Webb, S.J., 2014. Avoidable Euler errors - the use and abuse of Euler deconvolution applied to potential fields. Geophys. Prospect. 62, 1162–1168.

Reid, A.B., Thurston, J.B., 2014. The structural index in gravity and magnetic interpretation: errors, uses, and abuses. Geophysics 79 (4), J61–J66.

Ridsdill-Smith, T., Dentith, M., 1999. The wavelet transform in aeromagnetic processing. Geophysics 64 (4), 1003–1013.

Scheibe, L.F., Furtado, S.M.A., Comin-Chiaramonti, P., Gomes, C.B., 2005. Cretaceous alkaline magmatism from Santa Catarina state, southern Brazil. In: Comin-Chiaramonti, P., Gomes, C.B. (Eds.), Mesozoic to Cenozoic Alkaline Magmatism in the Brazilian Platform. Edusp/Fapesp, São Paulo, pp. 523–571.

Schmidt, P., Clark, D., Leslie, K., Bick, M., Tilbrook, D., Foley, C., 2004. GETMAG – a SQUID magnetic tensor gradiometer for mineral and oil exploration. Explor. Geophys. 35, 297–305.

Silva, J.B.C., Barbosa, V.C.F., 2003. 3D Euler deconvolution: theoretical basis for automatically selecting good solutions. Geophysics 68, 1962–1968.

Thompson, D.T., 1982. EULDPH: a new technique for making computer-assisted depth estimates from magnetic data. Geophysics 47, 31–37.

Ugalde, H., Morris, W.A., 2010. Cluster analysis of Euler deconvolution solutions: new filtering techniques and geologic strike determination. Geophysics 75 (3), L61–L70.

Uieda, L., Oilveira Jr., V.C., Barbosa, V.C.F., 2013. Modeling the Earth with fatiando a terra. In: Proceedings of the 12th Python in Science Conference (SciPy 2013), pp. 96–103.

Uieda, L., Oilveira Jr., V.C., Barbosa, V.C.F., 2014. Geophysical tutorial: euler deconvolution of potential-field data. Lead. Edge 33, 448–450.

Weihermann, J.D., Ferreira, F.J.F., Oliveira, S.P., de Souza, J., 2018. Magnetic interpretation of the Paranaguá Terrane, southern Brazil by signum transform. J. Appl. Geophys. 154, 116–127.